Journal of Materials Chemistry A

Accepted Manuscript

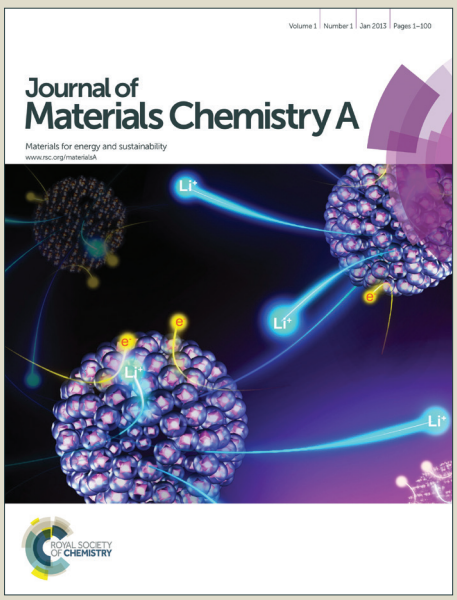

ROYAL SOCIETY OF CHEMISTRY

www.rsc.org/materialsA

Journal of Materials Chemistry A

PAPER

Origin of hydrogen evolution activity on MS_2 (M = Mo or Nb) monolayers†

Received 00th January 20xx,
Accepted 00th January 20xx

DOI: 10.1039/x0xx00000x

www.rsc.org/

Xiaobo Chen,*[a] Yu Gu,[a] Guohua Tao,[b] Yanli Pei,[c] Guangjin Wang,[d] and Ni Cui[a]

Catalytic activity often stems from surface atoms with dangling bonds. However, recent experiments shows that the perfect surfaces of two-dimensional transition-metal disulfide (TMD) nanosheets are highly active for hydrogen generation. On the basis of first-principles calculations, we find that the surface activity of MS_2 (M = Mo or Nb) monolayers largely originates from their bulk energy stabilization induced by electron injection in the Volmer reaction. A static computational model is proposed to refine the reaction Gibbs free energy of H adsorption into adiabatic electron and proton affinities for electronic-level thermodynamic description. It is found that the large adiabatic electron affinities of 1H-NbS_2, 1T-MoS_2 and 1T-NbS_2 monolayers lead to their strong H adsorption at low surface H coverage. In contrast, the negative adiabatic electron affinity of 1H-MoS_2 explains its catalytic inertness. For 1H-NbS_2, the large adiabatic electron affinity comes from the quenching of *d*-band exchange splitting after H adsorption and the stabilization of bonding frontier states. For 1T-MoS_2 and 1T-NbS_2, their large adiabatic electron affinities are ascribed to the stabilization effect of charge density waves. It is suggested that tensile strains or modifications that could increase the adiabatic electron affinity can enhance H adsorption on the basal-planes of TMDs.

I.Introduction

The hydrogen evolution reaction (HER), $H^+ + e^- \rightarrow 1/2H_2$, critical for hydrogen generation from water splitting, is catalyzed most effectively by Pt-group metals.[1] The growing interest in HER catalysis comes from the ongoing pursuit of hydrogen as a future energy carrier.[1, 2] Design and exploration of low cost and highly active HER catalysts to replace Pt-group metals are becoming a subject of fundamental interest.[3, 4] The lamellar transition-metal disulfides (TMDs) MS_2, where M is a transition-metal element of group IV, V or VI, have been attracting increasing interest in the applications of electrolysis of water because of their potential catalytic activity and abundance in the earth.[5-7] One archetype is MoS_2, which has been studied intensively, including a variety of structural forms like the triangular nanoparticles,[4, 8-11] the amorphous porous films,[12-16] the vertical multilayer structures[17, 18] and the molecular analogs,[19-22] etc. For all the structural forms, the HER catalytic activity originates from the edges of MoS_2, with the basal-planes catalytically inert due to weak H binding.[23] This conforms to the traditional notion that active sites of a catalyst are usually formed by unsaturated surface atoms with dangling bonds.[24] Based on density functional theory (DFT) calculations, however, Chen et. al. find that binding of H on the basal-plane sites of MoS_2 can be enhanced by 0.4 eV when MoS_2 is coupled with metal substrates.[25] Pan predicts that exothermic H adsorption occurs on the basal-planes of VS_2 and NbS_2 at low surface hydrogen coverage.[26] In experimental aspects, Voiry et. al. report that the distorted 1T phase of WS_2 nanosheets, as chemically exfoliated from the lithium-ion-intercalated bulk, exhibit excellent HER activity and facile electrode dynamics.[27] The onset overpotential can be reduced to below 100 mV and the Tafel slope reaches ca. 55 mV per decade. Similar enhancement is also found for the exfoliated 1T-MoS_2 nanosheets.[28, 29] Recently, a computational screening of two-dimensional TMD compounds points to more new 2D HER materials.[30] These works indicate that the HER activity is not restricted to unsaturated surface sites but also possible on perfect surfaces, which is particularly meaningful because perfect surfaces always have lower surface energy than truncated surfaces and therefore larger contact area with water. To date, however, the mechanisms for improved catalytic activity on the basal-planes of TMDs have not been understood.

Among all the TMDs, MoS_2 and NbS_2 are unique since they have the same triangular prismatic 2H structure under as-grown condition and both can transform into 1T phase when intercalated by lithium ions.[31, 32] Our previous work demonstrates that the formation of charge density waves (CDWs) and the maximization of chemical hardness occurred in 1T phase have significant influence on the electrochemical

[a]*Department of Physics and Siyuan Laboratory, College of Science and Engineering, Jinan University, Guangzhou 510632, China. Email: txbchen@jnu.edu.cn*
[b]*Shenzhen Key Laboratory of New Energy Materials by Design, Peking University, Shenzhen 518055, China.*
[c]*State Key Lab of Optoelectronics Materials & Technologies, School of Physics & Engineering, Sun Yat-Sen University, Guangzhou 510275, China.*
[d]*College of Chemistry and Materials Science, Hubei Engineering University, Xiaogan 432000, China.*
† Electronic Supplementary Information (ESI) available: See
DOI: 10.1039/x0xx00000x

reversibility of lithium ion batteries.[33] In addition, it is also demonstrated that the lack of one electron in the *d*-bands of NbS_2 leads to its significantly different electronic and magnetic properties.[31, 34, 35] These important properties are bulk relevant, but whether they can also influence the catalytic activity of the basal-planes is not clear. In this work, we develop a static computational model by first-principles calculations to trace the critical factors inducing surface activity of HER catalysts in general and the two-dimensional TMD nanosheets in particular. By investigating H adsorption on freestanding monolayers of MS_2 (M = Mo or Nb) in both 1H and 1T phases, it is found that the large electron affinities of 1T-MoS_2, 1H-NbS_2, and 1T-NbS_2 monolayers lead to their strong H adsorption on the basal-planes at low surface H coverage. On the contrary, the negative electron affinity of 1H-MoS_2 explains its catalytic inertness. By electronic structure calculations, we demonstrate that the different electron affinities of these monolayers are ascribed to their different stabilization mechanisms.

II. Models and Methods

HER can be described by the Volmer-Heyrovsky mechanism for MoS_2.[9, 36] The Volmer reaction, $H^+ + e^- + * \rightarrow H^*$, with * an adsorption site of the catalyst, is shown schematically in Fig. 1 (a). Electrons added to the catalyst recombine with protons at the interface between the catalyst and the electrolyte to form adsorbed H, a process that may involve the migration of electrons to the proton adsorption sites in general. Therefore, the overall Volmer reaction can be separated into a prior electron addition process and a subsequent proton adsorption, which is energetically more favorable than the opposite order.[37] As shown in Fig. 1 (b), the potential energy surfaces (PESs) I, II, and III correspond to the PESs of neutral, electron-charged, and hydrogenated catalysts respectively. A, C, and E indicate the respective equilibrium geometries. E_{ea} and E_{pa} are the vertical electron and proton affinities respectively. ε_{ea} and ε_{pa} are the respective reorganization energies of electron and proton addition processes. (E_{ea} + ε_{ea}) and (E_{pa} + ε_{pa}) are the adiabatic electron and proton affinities respectively. The negative sum of the adiabatic electron and proton affinities, $E_{A\rightarrow E}$ = – (E_{ea} + ε_{ea} + E_{pa} + ε_{pa}), for H addition to a catalyst is confirmed (Table S1) to be strictly equal to the hydrogen adsorption energy ΔE_H as calculated by

$$\Delta E_H = E(host + nH) - E(host + (n-1)H) - nE(H) \quad (1)$$

Here E(*host*+*nH*) and E(*H*) are the total energies of a catalyst host with *n* hydrogen atoms adsorbed, and an isolated H atom, respectively. By setting the reference potential to be that of the standard hydrogen electrode,[38] equation (1) becomes

$$\Delta E'_H = E(host + nH) - E(host + (n-1)H) - nE(H_2)/2 \quad (2)$$

where $E(H_2)$ is the total energy of a hydrogen gas molecule. The difference between $\Delta E'_H$ and ΔE_H (ΔE_{cp} = $\Delta E'_H$ – ΔE_H) reflects the difference in H chemical potential between the

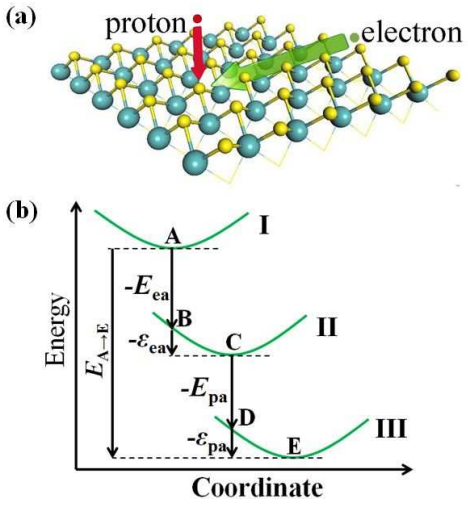

Fig. 1. (Color online) (a) A schematic chart for an electron injection followed by a proton adsorption on the surface of a catalyst host. (b) Potential energy surfaces (PESs) describing the catalytic system at the different states. The abscissa label 'coordinate' refers to the ionic nuclear configuration. Energy changes between different PESs follow the route indicated by A, B, C, D, and E.

free atom (ion) state and the molecular state. The reaction free energy $\Delta G = \Delta E'_H + \Delta E_{ZPE} - T\Delta S_H$ can be rewritten as[39]

$$\Delta G = -(E'_{ea} + E'_{pa}) + \Delta E_{ZPE} - T\Delta S_H + \Delta E_{cp} \quad (3)$$

where E'_{ea} = E_{ea} + ε_{ea} and E'_{pa} = E_{pa} + ε_{pa} are the adiabatic electron affinity and proton affinity, respectively, which depend on the surface H coverage. ΔE_{cp} and $T\Delta S_H$ are 3.380 and -0.205 eV, respectively, calculated at the PBE level (Table S2). ΔE_{ZPE} is the difference of zero point energy of H between the adsorbed state and the molecular state, which is only weakly dependent on materials (Table S2). Therefore, ΔG for different materials are distinguished primarily by their different E'_{ea} and E'_{pa}. We calculate E'_{ea} and E'_{pa} by

$$E'_{ea} = E(n, \mathrm{N}) - E(n+1, \mathrm{N}) \quad (4)$$

$$E'_{pa} = E(n+1, N) - E(n+1, N+1) \quad (5)$$

for one electron and one proton addition, respectively. Here all the energies at the right hand of equation (4) and (5) correspond to the geometries of full structural relaxation. *n* and N are the numbers of valence electrons and protons involved in the system, respectively. Note that VASP treats the total energy of a system with respect to the atomic energy in reference configuration (*i.e.* the configuration for which the pseudopotential is generated). For comparisons of experimental E'_{pa} with our calculated ones, one should add the atomic reference energy of H (*ca.* 12.49 eV) into the E'_{pa} calculated by Eq (5). Decomposition of the H adsorption energy in Eq (3) to the adiabatic electron and proton affinities gives a quantitative description of the individual electron and proton processes in the Volmer reaction. This model links the reaction free energy ΔG, a measure of the overpotential, to the intrinsic electronic properties of a compound. Both E'_{ea}

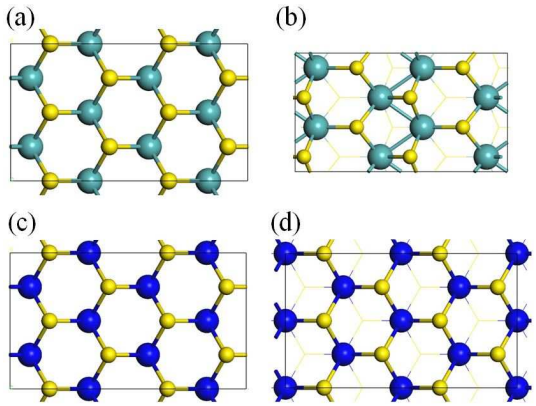

Fig. 2. (Color online) Top view of optimized monolayer structures for (a) 1H-MoS_2, (b) 1T-MoS_2, (c) 1H-NbS_2, and (d) 1T-NbS_2. The 1T-MoS_2 monolayer is in the y-z plane and the other monolayers are in the *x-y* plane. Mo, Nb, and S atoms are indicated by green, blue and yellow balls, respectively. For (b) and (d), the bottom S atoms and their bonds are represented by weak lines so as to clearly show the upper atoms.

and E'_{pa} can be determined by theoretical and experimental methods and thus can be used to trace the electronic nature of H adsorption on different materials, and furthermore to design, screen, and optimize the catalytic properties of a catalyst. For clarity, we use terminologies involving 'hydrogen' or its abbreviation 'H' to refer to the total effect of electron addition and proton adsorption. This applies for the cases where only the total reactive thermodynamics, e.g. ΔG, ΔE_H, or $\Delta E'_H$, are concerned; while for E'_{ea} or E'_{pa}, we will explicitly indicate the individual electron or proton process instead.

The starting structures of MS_2 (M = Mo and Nb) are constructed by extracting a monolayer from their bulk counterparts[31, 40, 41] and then adding a vacuum region of 15 Å to separate neighboring layers. To study hydrogen adsorption on a MS_2 monolayer at different hydrogen coverage, we use a rectangle super cell defined by lattice vectors of [210], [010] and [001], which consists of 8 MS_2 formula units. hydrogen atoms are adsorbed on the top of S atoms, where is the most stable position. There are totally 8 S sites available for hydrogen adsorption on each side of monolayer and the full hydrogen coverage refers to one hydrogen atom per S atom is adsorbed on one side. For all the structures, the in-plane lattice parameters are fully relaxed, while the *c* axis height is fixed. We carry out the Density-functional theory (DFT) calculations by using the Vienna Ab-initio Simulation Package (VASP).[42] Interactions of electrons with ion cores are represented by the projector augmented wave (PAW) potential.[43, 44] The generalized gradient approximation (GGA) parameterized by Perdew, Burke and Ernzerhof (PBE) is used for the exchange-correlation functional.[45] A cutoff energy of 400 eV and a Monkhorst-Pack special mesh of 4×8×1 are used for all the supercells. Full structural relaxations are performed until all the forces acting on all the ions are smaller than 0.02 eV/Å. Spin polarization is included for all cases. The finite difference method is used for calculations of oscillation frequencies and zero point energies. For the electronic entropy contribution, a Methfessel-Paxton thermal smearing with a width of 0.01 eV is used and extrapolated to zero.

III. Results and Discussion

The optimized structures for all the monolayers are presented in Fig. 2 (a) – (d). After relaxation, all the monolayers expand slightly relative to their bulk counterparts. The two 1H super cells (1H-MoS_2 and 1H-NbS_2) and the 1T-NbS_2 super cell keep orthogonal with atoms remaining in the same structural motif as in their bulk. The 1T-MoS_2 becomes monoclinic with a space group of $P12_1/M1$. However, the in-plane lattice remains rectangular with an obvious zigzag-type Mo plane distortion, consistent with the experimental findings.[27, 46] This Mo plane distortion is associated with the formation of CDWs.[40] The 1T-NbS_2 monolayer, however, does not present any distortion after optimization. The calculated structural parameters (Table S3) of the corresponding unit cells are summarized in Table S3, which are in agreement with the available theoretical and experimental results. Fig. S1 (e) – (h) shows the most stable hydrogenated configurations with 1/8 hydrogen coverage, *i. e*. one hydrogen atom per supercell. For 1H-MoS_2, no observable structural changes occurs after hydrogen adsorption. The angle between the S-H bond and the basal plane is *ca*. 65°. For 1T-MoS_2, the angle becomes 74° but the structure distorts further, leading to complete losing of symmetry. For 1H-NbS_2 and 1T-NbS_2, slight structural distortion occurs around the hydrogen atom.

Fig. 3 (a) shows the free energy ΔG as a function of hydrogen coverage for all the four considered structures. A positive ΔG indicates weak and endothermic hydrogen binding, while a negative ΔG indicates strong and exothermic hydrogen adsorption. At 1/8 H coverage, a MoS_2 monolayer presents endothermic adsorption of H with a large positive overpotential of ca. 1.91 eV, consistent with the experimental observation that basal-plane sites of MoS_2 are catalytically inert.[23] When H coverage increases to 3/8, the S-H binding enhances by ca. 0.78 eV, although the overpotential is still very large. For higher H coverage, the structure presents repelling state and H atoms are excluded into the vacuum region. In contrast to 1H-MoS_2, all the other monolayer disulfides have much stronger H adsorption at low H coverage and their ΔG increase when H coverage increases. At the lowest H coverage 1/8, ΔG are 0.03, -0.12, and 0.06 eV for 1T-MoS_2, 1H-NbS_2 and 1T-NbS_2 respectively. When H coverage decreases further to 1/16 (not shown) by doubling the supercell size along the y direction, ΔG become 0.02, -0.15, and -0.24 eV for 1T-MoS_2, 1H-NbS_2 and 1T-NbS_2 respectively. This indicates that 1) 1T-MoS_2 is hard to exothermically adsorb H atoms even at very low H coverage, consistent with the experiment that unstrained 1T-WS_2 (or 1T-MoS_2) exhibits small catalysis current;[27] and 2) 1H-NbS_2 and 1T-NbS_2 could present further enhanced H adsorption with lowering H coverage. Nevertheless, 1T-MoS_2, 1H-NbS_2 and 1T-NbS_2 monolayers all exhibit much stronger H adsorption ability with reaction overpotential close to the zero equilibrium overpotential at low H coverage, indicating their good potential for practical applications. Note that a more positive ΔG of 0.06 eV is obtained for 1H-NbS_2 at 1/12 H coverage in Pan's work.[26] This is because he assumes the same $\Delta E_{ZPE} - T\Delta S_H$ (0.24 eV) as that

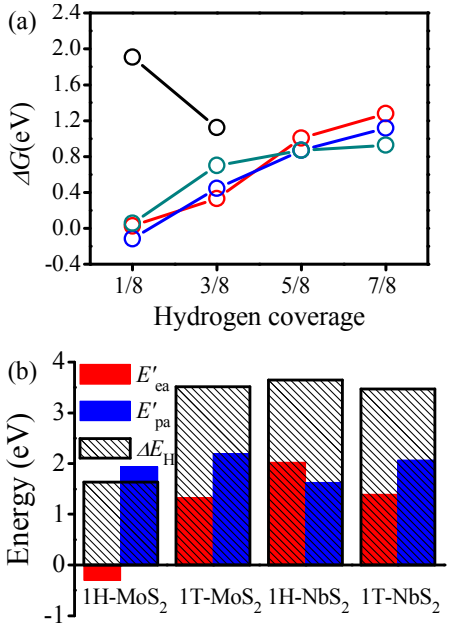

Fig. 3. (Color online) (a) Reaction free energy ΔG as a function of H coverage for 1H-MoS_2 (black symbols), 1T-MoS_2 (red symbols), 1H-NbS_2 (blue symbols), and 1T-NbS_2 (green symbols) monolayers. (b) Adiabatic electron affinity E'_{ea}, proton affinity E'_{pa}, and hydrogen adsorption energy ΔE_H (black symbols) for different monolayer disulfides. The proton affinities E'_{pa} have subtracted the atomic reference energy of H (*ca*. 12.49 eV), which should be added if comparisons between experimental and calculated E'_{pa} are needed.

used for noble metals.[39] Our calculations based on the finite difference method show that ΔE_{ZPE} - $T\Delta S_H$ is only 0.16 eV for 1H-MoS_2 and 0.15 eV for 1H-NbS_2 (Table S2). In addition, the in-plane lattice parameters are relaxed in our work but fixed in Pan's work, also responsible for the difference. In the following, all the analysis is focused on the lowest H coverage 1/8.

The strong H adsorption on 1T-MoS_2, 1H-NbS_2 and 1T-NbS_2 at low H coverage can be understood from the contribution of electron and proton affinities. In Fig. 3 (b), we plot E'_{ea}, E'_{pa} , and ΔE_H for the four pristine compounds. The hydrogen adsorption energy ΔE_H, which is exactly equal to the sum of E'_{ea} and E'_{pa} as aforementioned, contributes to the main parts of ΔG according to Eq. (3). The larger the ΔE_H is, the stronger the H adsorption will be. Compared to the case of 1H-MoS_2, all the other monolayers have much larger ΔE_H, accounting for their stronger H adsorption ability. Note that E'_{pa} differs by only *ca*. 0.56 eV for the four monolayers, whereas E'_{ea} differs by nearly 2.33 eV, indicating that the adiabatic electron affinity E'_{ea} is the primary factor leading to the different H adsorption ability. In general, E'_{pa} is primarily related to the electronegativity and coordination numbers of surface anions,[47] which are identical for all the monolayers. Therefore, E'_{pa} varies not very large. In contrast, E'_{ea} is affected more by the electronic structure of bulk, which could differ remarkably for different transition-metal disulfides. Although for a monolayer, the bulk is constituted by only one transition-metal atom plane, the PES model used here indicates that the catalytic activity is not only surface relevant but rather determined by the bulk properties. Particularly, E'_{ea} reflects

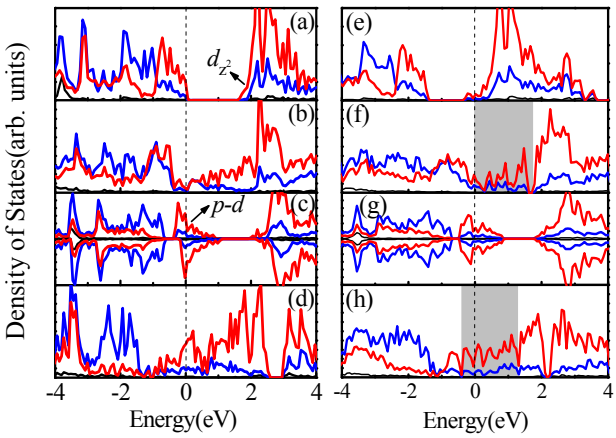

Fig. 4. (Color online) Projected density of states for the pristine monolayer structures: (a) 1H-MoS_2, (b) 1T-MoS_2, (c) 1H-NbS_2, and (d) 1T-NbS_2, and the hydrogenated structures of 1/8 H coverage: (e) 1H-MoS_2H_1, (f) 1T-MoS_2H_1, (g) 1H-NbS_2H_1, and (h) 1T-NbS_2H_1. *s*, *p*, and *d* states are indicated by black, blue and red curves, respectively. (c) and (g) are shown with spin-polarized density of states, with the upper panel spin-up and the lower panel spin-down. The Fermi level is indicated by the dotted line. The grey shadowed regions indicate *d*-band localization after H adsorption.

the ability of a catalyst as a whole to accept electrons. The larger the E'_{ea} is, the more electrons a catalyst could accept. A negative E'_{ea} of 1H-MoS_2 indicates that electrons are rather difficult to be injected, which may prevent succeeding proton adsorption. On the contrary, the much larger E'_{ea} for the other disulfides indicates that they have much more facile electrode dynamics, consistent with the experimental findings.

According to the definition of Eq (4), a positive E'_{ea} indicates energy stabilization after electron injection, while a negative one indicates destabilization of the system. Therefore, the emergency of surface catalytic activity is closely related to the stabilization of bulks. To investigate the stabilization mechanisms, we calculate the projected density of states (PDOS) for the four monolayers before and after one H atom is adsorbed per super cell, which primarily reflects the PDOS curves before and after one electron is added. The charge density of the frontier states, *i. e*. the lowest unoccupied states, are also presented for the pristine structures in Fig. 5 because of their relevance to chemical activity. It is seen from Fig. 4 (a) that 1H-MoS_2 is a semiconductor with a band gap of *ca*. 1.8 eV, in agreement with previous theoretical and experimental reports.[48, 49] The conduction band minimum (CBM) is dominated by the antibonding d_{z^2} state, as could be confirmed by the dumbbell-shaped charge distribution around Mo sites and the charge exhaustion between Mo and S in Fig. 5 (a). After one electron is added, the antibonding CBM is filled, which destabilizes the system and thus results in the negative E'_{ea} of 1H-MoS_2.

Although structurally similar to 1H-MoS_2, 1H-NbS_2 is a metal. Fig. 4 (c) shows that the upper valence band is half-filled since Nb-4*d* has one electron less than Mo-4*d*. The frontier states are therefore featured by *p-d* covalent bonding characteristic. This can be confirmed by Fig. 5 (b), where electrons accumulate in between Nb and S ions. The bonding characteristic of the frontier states are favorable for energy

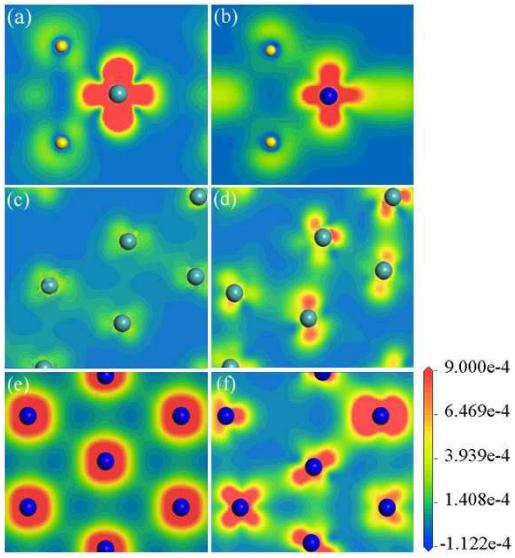

Fig. 5. (Color online) Partial charge density of the lowest unoccupied states. The energy range is from the Fermi energy E_f to (E_f + 0.1) eV. The field range is from -1.12×10^{-4} to 9.00×10^{-4}. (a) and (b) are the *x*-*z* planar charge density for the pristine 1H-MoS_2 and 1H-NbS_2 monolayers, respectively. (c) and (d) are the *x*-*y* planar (the Mo plane) charge density for the pristine 1T-MoS_2 monolayer and its hydrogenated counterpart with 1/8 H coverage, respectively. (e) and (f) are the *x*-*y* planar (the Nb plane) charge density for the pristine 1T-NbS_2 monolayer and its hydrogenated counterpart with 1/8 H coverage, respectively. The sites of Mo, Nb and S are indicated by green, blue and yellow balls, respectively.

stabilization when electrons are added, and therefore partially responsible for the large E'_{ea}. In addition, note that an evident exchange splitting exists in the PDOS of the pristine 1H-NbS_2, which produces a magnetic moment of 0.27μ_B per formula unit (*f. u.*). After one H atom is adsorbed, the magnetic moment is nearly quenched, as seen from Fig. 4 (g). This also contributes to the system stabilization and the large E'_{ea} of 1H-NbS_2.

1T-MoS_2 is also metallic, as seen from Fig. 4 (b). The DOS in the range of (0, 2) eV is contributed mainly by the *d*-*d* interaction of neighbouring Mo ions along the zigzag line and partially by the Mo-S *p*-*d* bonding.[31, 50] Enhancement of the *d*-*d* interaction can lead to enhanced electron correlation, which is crucial for the formation of CDWs in bulk TMDs.[51] Fig. 5 (c) shows the charge density of the frontier states for the pristine 1T-MoS_2 monolayer. Evident *d*-*d* interaction in the Mo plane can also be observed, although not very strong. The charge density of the hydrogenated monolayer with 1/8 H coverage is presented in Fig. 5 (d). It is seen that the charge density on Mo sites increases significantly and the neighbouring *d*-*d* interaction enhances. This leads to enhanced *d*-electron correlation with Hubbard-type localization, as confirmed by Fig. 4 (f). The *d*-band peaks are narrowed and enhanced after H adsorption. As a result, the system is stabilized and a large E'_{ea} (1.33 eV) is generated. The *d*-band localization, determining the strength of electron correlation,[51] becomes more remarkable when H coverage reaches 100%, where a large band gap of *ca*. 1 eV opens (see Fig. S2). This is similar to the Mott-Hubbard-type metal-to-insulator transition induced by lithium ion intercalation in the bulk counterpart.[31]

The case is very similar for 1T-NbS_2. Comparison of Fig. 4 (d) and (h) suggests that electron injection also leads to *d*-band localization. When H coverage increases, the localization becomes more evident (Fig. S3). Fig. 5 (e) and (f) shows the charge density before and after one H atom is adsorbed. For the pristine structure, an isotropic *d*-*d* interaction exists among neighboring Nb ions. After one H atom is adsorbed, the *d*-*d* interaction enhances and becomes anisotropic, which leads to Nb plane distortion. When H coverage increases, this anisotropic interaction enhances further and the Nb plane distortion aggravates, which finally leads to the formation of CDWs similar to the bulk case.[31] This stabilization mechanism associated with the formation of CDWs is also similar to that of the 1T-MoS_2 monolayer, accounting for their similar E'_{ea}.

From the above analysis, one can see that different stabilization mechanisms lead to different E'_{ea}, which further leads to different surface catalytic activity for the four monolayers. The stabilization brought by CDWs leads to enhancement of H adsorption on the 1T phases of MoS_2 and NbS_2. However, it also leads to localization of *d*-bands above the Fermi energy, which could increase the electric resistance and retard the electrode dynamics. This is particular serious when H coverage is high, because strong localization may lead to band gap opening and a metal-to-insulator transition. In contrast, the stabilization induced by the quenching of *d*-band exchange splitting and the filling of the bonding frontier states does not bring about remarkable localization in 1H-NbS_2. However, with the increase of H coverage, the Fermi energy shifts up in energy. This may also lead to a metal-to-insulator transition when the upper valence bands are full filled.[26] Consequently, 1H-NbS_2, 1T-MoS_2 and 1T-NbS_2 monolayers are only applicable for catalysis at low surface H coverage, indicating that the effective active sites are scarce. Note that a recent work relates the difference of surface catalytic activity of disulfides between 1H and 1T phases to the position of S-*p* band.[30] Our calculations take the theoretical analysis one step further by explicitly including adiabatic electron and proton affinities to more quantitatively characterize the underlying catalytic mechanisms.

Another important effect should be considered is the support interactions. A previous work suggests that strong support interactions may weaken H binding on the edges of MoS_2 since the support play a role of electron doping.[52] Similarly, any support that serves as an electron donor may affect H adsorption on the basal plane of TMDs. This could be inferred from the above analysis of electronic states. For the 1H-NbS_2 monolayer, a donor-type support may diminish the intrinsic exchange splitting, resulting in decrease of E'_{ea}. As a result, the subsequent recombination of protons from the electrolyte and electrons from the external circuit could be retarded. For 1T-MoS_2 and 1T-NbS_2 monolayers, a donor-type support may induce the stabilization of CDWs in the materials *before* electrons are injected from the external circuit, which could also lead to decrease of E'_{ea} and then hamper the recombination of protons and external electrons. Consequently, acceptor-type or neutral supports are more preferable for the purpose of keeping the large E'_{ea} and

facilitating the Volmer reaction. Here, one sees that the major impact of supports on the basal-plane catalysis is by changing the adiabatic electron affinity of the catalyst. This is different from the case of MoS_2-edge catalysis, where edge reconstruction can be induced and therefore the adiabatic proton affinity can be changed by the support.[52] More detailed understanding on the support effect needs further studies.

Conclusions

In summary, first-principles calculations have been carried out to study H adsorption on the monolayers of MS_2 (M = Mo or Nb) in both 1H and 1T phases. It is demonstrated that the surface activity of MS_2 largely originates from their bulk stabilization. A static computational model is proposed to trace the stabilization mechanism by decomposing the reaction free energy ΔG into the contributions of electron and proton affinities. It is found that the large adiabatic electron affinities of 1H-NbS_2, 1T-MoS_2 and 1T-NbS_2 monolayers lead to strong H adsorption on their basal-planes at low surface H coverage. In contrast, the negative adiabatic electron affinity of 1H-MoS_2 explains its catalytic inertness. For 1H-NbS_2, quenching of the large exchange splitting of *d*-bands after H adsorption and the stabilization of the bonding frontier states leads to the large adiabatic electron affinity. For 1T-MoS_2 and 1T-NbS_2, their large adiabatic electron affinities are induced by CDWs. It is suggested that acceptor-type or neutral supports are favorable for the basal-plane catalysis since the adiabatic electron affinity will not be reduced. All the above stabilization mechanisms are bulk-related and can be primarily described by the adiabatic electron affinity E'_{ea}. Since no additional limits have been involved in the deduction of the computational model, the approach used in this work is applicable for studying other catalytic systems or materials. However, for comparisons between materials with different anions, e. g. sulphides and selenides, the contribution of E'_{pa} to their activity difference may become more significant and the catalytic mechanism probably becomes more complicated. In that case, both E'_{ea} and E'_{pa} should be fully considered in order to determine the catalytic mechanism.

Finally, we suggest that any modification that increases the adiabatic electron affinity of a two-dimensional TMD material can enhance H adsorption. The recent utilization of tensile strain to enhance the HER activity of 1T-WS_2 is in support of this viewpoint. The tensile strain destabilizes the CDW state in the pristine nanosheets, which leads to increase of $E(n, \mathrm{N})$ in Eq (4) and therefore the increase of the adiabatic electron affinity E'_{ea}. The strain effect will be discussed in detail in our future work. The insights obtained in the present work may prove to be instrumental in understanding the nature of catalytic activity on perfect surfaces and in designing new two-dimensional catalysts with large contact area with water.

Acknowledgements

Shanghai Supercomputer Center and Ms. Yuanyuan Zhao are thanked for providing computational resources and technical support. This work was supported by the National Natural Science Foundation of China (21303237, 11404142, 11147147), the Natural Science Foundation of Zhejiang Province (LQ12A04004), the Natural Science Foundation of Hubei Province (2015CFC769), the Distinguished Young Talents in Higher Education of Guangdong (LYM11021, 21612439), and the Shenzhen Science and Technology Innovation Council (Grant No. ZDSY20130331145131323).

References

1. P. D. Tran and J. Barber, *Phys. Chem. Chem. Phys.*, 2012, **14**, 13772-13784.
2. M. G. Walter, E. L. Warren, J. R. McKone, S. W. Boettcher, Q. Mi, E. A. Santori and N. S. Lewis, *Chem. Rev.*, 2010, **110**, 6446-6473.
3. J. K. Norskov, T. Bligaard, J. Rossmeisl and C. H. Christensen, *Nat Chem*, 2009, **1**, 37-46.
4. B. Hinnemann, P. G. Moses, J. Bonde, K. P. Jørgensen, J. H. Nielsen, S. Horch, I. Chorkendorff and J. K. Nørskov, *J. Am. Chem. Soc.*, 2005, **127**, 5308-5309.
5. A. B. Laursen, S. Kegnaes, S. Dahl and I. Chorkendorff, *Energy Environ. Sci.*, 2012, **5**, 5577-5591.
6. M. Chhowalla, H. S. Shin, G. Eda, L.-J. Li, K. P. Loh and H. Zhang, *Nat. Chem.*, 2013, **5**, 263-275.
7. D. Chen, W. Chen, L. Ma, G. Ji, K. Chang and J. Y. Lee, *Mater. Today*, 2014, **17**, 184-193.
8. J. Kibsgaard, J. V. Lauritsen, E. Lægsgaard, B. S. Clausen, H. Topsøe and F. Besenbacher, *J. Am. Chem. Soc.*, 2006, **128**, 13950-13958.
9. Y. Li, H. Wang, L. Xie, Y. Liang, G. Hong and H. Dai, *J. Am. Chem. Soc.*, 2011, **133**, 7296-7299.
10. Q. Xiang, J. Yu and M. Jaroniec, *J. Am. Chem. Soc.*, 2012, **134**, 6575-6578.
11. E. G. S. Firmiano, M. A. L. Cordeiro, A. C. Rabelo, C. J. Dalmaschio, A. N. Pinheiro, E. C. Pereira and E. R. Leite, *Chem. Commun.*, 2012, **48**, 7687-7689.
12. H. Vrubel, D. Merki and X. Hu, *Energy Environ. Sci.*, 2012, **5**, 6136-6144.
13. D. Merki, S. Fierro, H. Vrubel and X. Hu, *Chem. Sci.*, 2011, **2**, 1262-1267.
14. D. Merki and X. Hu, *Energy Environ. Sci.*, 2011, **4**, 3878-3888.
15. T. Wang, L. Liu, Z. Zhu, P. Papakonstantinou, J. Hu, H. Liu and M. Li, *Energy Environ. Sci.*, 2013, **6**, 625-633.
16. T. Wang, J. Zhuo, K. Du, B. Chen, Z. Zhu, Y. Shao and M. Li, *Adv. Mater.*, 2014, **26**, 3761-3766.
17. J. Kibsgaard, Z. Chen, B. N. Reinecke and T. F. Jaramillo, *Nat. Mater.*, 2012, **11**, 963-969.
18. D. Kong, H. Wang, J. J. Cha, M. Pasta, K. J. Koski, J. Yao and Y. Cui, *Nano Lett.*, 2013, **13**, 1341-1347.
19. Y. Hou, B. L. Abrams, P. C. K. Vesborg, M. E. Björketun, K. Herbst, L. Bech, A. M. Setti, C. D. Damsgaard, T. Pedersen, O. Hansen, J. Rossmeisl, S. Dahl, J. K.

Nørskov and I. Chorkendorff, *Nat Mater*, 2011, **10**, 434-438.
20. T. F. Jaramillo, J. Bonde, J. Zhang, B.-L. Ooi, K. Andersson, J. Ulstrup and I. Chorkendorff, *J. Phys. Chem. C*, 2008, **112**, 17492-17498.
21. B. Keita, S. Floquet, J.-F. Lemonnier, E. Cadot, A. Kachmar, M. Benard, M.-M. Rohmer and L. Nadjo, *J. Phys. Chem. C*, 2008, **112**, 1109-1114.
22. H. I. Karunadasa, E. Montalvo, Y. Sun, M. Majda, J. R. Long and C. J. Chang, *Science*, 2012, **335**, 698-702.
23. T. F. Jaramillo, K. P. Jørgensen, J. Bonde, J. H. Nielsen, S. Horch and I. Chorkendorff, *Science*, 2007, **317**, 100-102.
24. T. Bligaard, J. K. Nørskov and B. I. Lundqvist, in *Handbook of Surface Science*, eds. E. Hasselbrink and B. I. Lundqvist, North-Holland, 2008, vol. Volume 3, pp. 269-340.
25. W. Chen, E. J. G. Santos, W. Zhu, E. Kaxiras and Z. Zhang, *Nano Lett.*, 2013, **14**, 1381-1387.
26. H. Pan, *Sci. Rep.*, 2014, **4**, 5348.
27. D. Voiry, H. Yamaguchi, J. Li, R. Silva, D. C. B. Alves, T. Fujita, M. Chen, T. Asefa, V. B. Shenoy, G. Eda and M. Chhowalla, *Nat. Mater.*, 2013, **12**, 850-855.
28. M. A. Lukowski, A. S. Daniel, F. Meng, A. Forticaux, L. Li and S. Jin, *J Am. Chem. Soc.*, 2013, **135**, 10274-10277.
29. H. Wang, Z. Lu, D. Kong, J. Sun, T. M. Hymel and Y. Cui, *ACS Nano*, 2014, **8**, 4940-4947.
30. M. Pandey, A. Vojvodic, K. S. Thygesen and K. W. Jacobsen, *J. Phys. Chem. Lett.*, 2015, **6**, 1577-1585.
31. R. H. Friend and A. D. Yoffe, *Adv. Phys.*, 1987, **36**, 1-94.
32. J. A. Wilson and A. D. Yoffe, *Adv. Phys.*, 1969, **18**, 193-335.
33. X. Chen, J. He, D. Srivastava and J. Li, *Appl. Phys. Lett.*, 2012, **100**, 263901-263904.
34. V. V. Ivanovskaya, A. Zobelli, A. Gloter, N. Brun, V. Serin and C. Colliex, *Phys. Rev. B*, 2008, **78**, 134104.
35. Y. Zhou, Z. Wang, P. Yang, X. Zu, L. Yang, X. Sun and F. Gao, *ACS Nano*, 2012, **6**, 9727-9736.
36. B. E. Conway and B. V. Tilak, *Electrochim. Acta*, 2002, **47**, 3571-3594.
37. Y. Huang, R. J. Nielsen, W. A. Goddard and M. P. Soriaga, *J. Am. Chem. Soc.*, 2015, **137**, 6692-6698.
38. J. K. Nørskov, J. Rossmeisl, A. Logadottir, L. Lindqvist, J. R. Kitchin, T. Bligaard and H. Jónsson, *J. Phys. Chem. B*, 2004, **108**, 17886-17892.
39. J. K. Nørskov, T. Bligaard, A. Logadottir, J. R. Kitchin, J. G. Chen, S. Pandelov and U. Stimming, *J. Electrochem. Soc.*, 2005, **152**, J23-J26.
40. X. Rocquefelte, F. Boucher, P. Gressier, G. Ouvrard, P. Blaha and K. Schwarz, *Phys. Rev. B*, 2000, **62**, 2397-2400.
41. J. Heising and M. G. Kanatzidis, *J. Am. Chem. Soc.*, 1999, **121**, 638-643.
42. G. Kresse and J. Furthmüller, *Phys. Rev. B*, 1996, **54**, 11169-11186.
43. P. E. Blöchl, *Phys. Rev. B*, 1994, **50**, 17953-17979.
44. G. Kresse and D. Joubert, *Phys. Rev. B*, 1999, **59**, 1758-1775.
45. J. P. Perdew, K. Burke and M. Ernzerhof, *Phys. Rev. Lett.*, 1996, **77**, 3865-3868.
46. R. A. Gordon, D. Yang, E. D. Crozier, D. T. Jiang and R. F. Frindt, *Phys. Rev. B*, 2002, **65**, 125407.
47. J. L. Reed, *J. Phys. Chem.*, 1994, **98**, 10477-10483.
48. K. Mak, C. Lee, J. Hone, J. Shan and T. Heinz, *Phys. Rev. Lett.*, 2010, **105**, 136805.
49. S. Lebègue and O. Eriksson, *Phys. Rev. B*, 2009, **79**.
50. X. Chen, Z. Chen and J. Li, *Chin. Sci. Bull.*, 2013, **58**, 1632-1641.
51. Z. Zhu, Y. Cheng and U. Schwingenschlögl, *Phys. Rev. B*, 2012, **85**, 245133.
52. C. Tsai, F. Abild-Pedersen and J. K. Nørskov, *Nano Lett.*, 2014, **14**, 1381-1387.

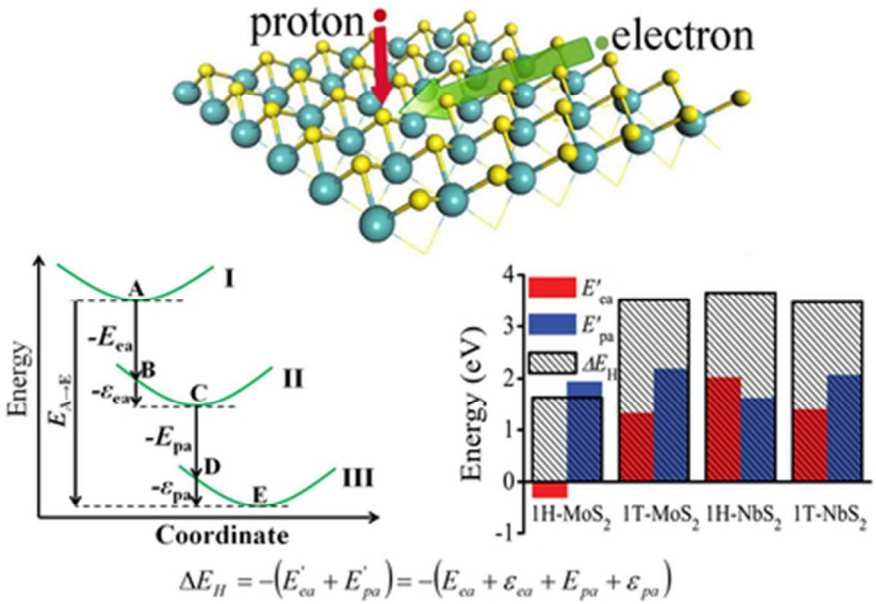

$$\Delta E_H = -\left(E'_{ea} + E'_{pa}\right) = -\left(E_{ea} + \varepsilon_{ea} + E_{pa} + \varepsilon_{pa}\right)$$

39x25mm (300 x 300 DPI)